

# Universal Reconstruction of Complex Magnetic Profiles with Minimum Prior Assumptions

Changyu Yao<sup>1,\*</sup>, Yinyao Shi<sup>1,\*</sup>, Ji-In Jung<sup>2</sup>, Zoltán Váci<sup>3</sup>, Yizhou Wang<sup>1</sup>, Zhongyuan Liu<sup>1</sup>, Yue Yu<sup>1</sup>, Chuanwei Zhang<sup>1,4</sup>, Sonia Tikoo-Schantz<sup>2</sup>, Chong Zu<sup>1,4,5,†</sup>

<sup>1</sup>Department of Physics, Washington University, St. Louis, MO 63130, USA

<sup>2</sup>Department of Geophysics, Stanford University, Stanford, CA 94305, USA

<sup>3</sup>Department of Earth and Planetary Sciences, Washington University, St. Louis, MO 63130, USA

<sup>4</sup>Center for Quantum Leaps, Washington University, St. Louis, MO 63130, USA

<sup>5</sup>Institute of Materials Science and Engineering, Washington University, St. Louis, MO 63130, USA

\*These authors contributed equally to this work

†To whom correspondence should be addressed; E-mail: zu@wustl.edu

(Dated: December 2, 2024)

Understanding the intricate magnetic structures of materials is crucial for the advancements in material science, spintronics, and geology. Recent developments of quantum-enabled magnetometers, such as nitrogen-vacancy (NV) centers in diamond, have enabled direct imaging of magnetic field distributions associated with a wide variety of magnetic profiles. However, reconstructing the magnetization of a sample from a measured magnetic field map poses a complex inverse problem, which can be further complicated by the presence of measurement noise, finite spatial resolution, and the sample-to-sensor distance. In this work, we introduce a novel and efficient GPU-based method for reconstructing magnetic source quantities (i.e. spatially varying magnetization density) from measured magnetic fields with minimum prior assumptions. We validate our method by simulating diverse magnetic structures under realistic experimental conditions, including multi-domain ferromagnetism and magnetic spin textures such as skyrmion, anti-skyrmion, and meron. Experimentally, we apply our technique to investigate the magnetic field maps from a lunar rock (Apollo lunar mare basalt sample 10003,184) obtained using a wide-field quantum diamond microscope. The reconstructed magnetic domains of the lunar rock are consistent with current paleomagnetic knowledge. Our approach provides a versatile and universal tool for investigating complex magnetization profiles, paving the way for future quantum sensing experiments.

## INTRODUCTION

Characterizing complex magnetic profiles is essential for understanding the fundamental mechanisms of magnetic materials and geological samples, as well as for advancing next-generation spintronics technology [1–3]. Quantum-enabled magnetometers have made significant advancements in probing the local magnetic field distribution with unprecedented accuracy and resolution [4, 5]. Existing quantum systems include, for example, atomic vapors [6–12], nitrogen-vacancy (NV) centers in diamond [5, 13–21] and spin defects in two-dimensional materials [22–27], and superconducting quantum interference devices (SQUIDs) [28–32]. Their diverse applications encompass exploring magnetic properties in materials [14, 33–36], biological processes [5, 37–39], geological samples [3, 40–43], among others.

Accurate reconstruction of magnetic profiles from the measured field map presents a challenging inverse problem. In reality, the presence of experimental measurement noise, finite imaging resolution, and sample-to-sensor distance will further complicate the reconstruction process. Current methods include inverse Fourier transformation [44–46], moment reconstruction [40, 41, 47], and machine learning techniques [48]. Each of these approaches has its own limitations. The inverse Fourier

transformation is commonly employed for reconstructing current density rather than magnetization. When used to solve for magnetization, the approach requires the prior assumption of a fixed axis along which the magnetization is constrained, a requirement that is often inapplicable in various scenarios [34–36, 49]. The moment reconstruction method limits the sample as a point magnetic multiple, losing the spatial structure of the underlying magnetization. Meanwhile, the machine learning approach requires extensive computational resources and large training datasets to accurately capture the full range of physical phenomena.

In this work, we present three main results. First, we develop a GPU-accelerated computational model capable of reconstructing the full spatially varying magnetization from three-dimensional magnetic field maps (Figure 1). To guide the optimization process for various complex magnetic profiles existing in nature, we introduce a customizable physics-informed loss function and implement the stochastic directional Newton method to efficiently drive the reconstruction process. Second, we validate our method through the simulations of various magnetic structures, including multi-domain ferromagnetism and topological spin textures such as skyrmion, anti-skyrmion, and meron under realistic experimental conditions (Figure 2 and Figure 3). In particular, by



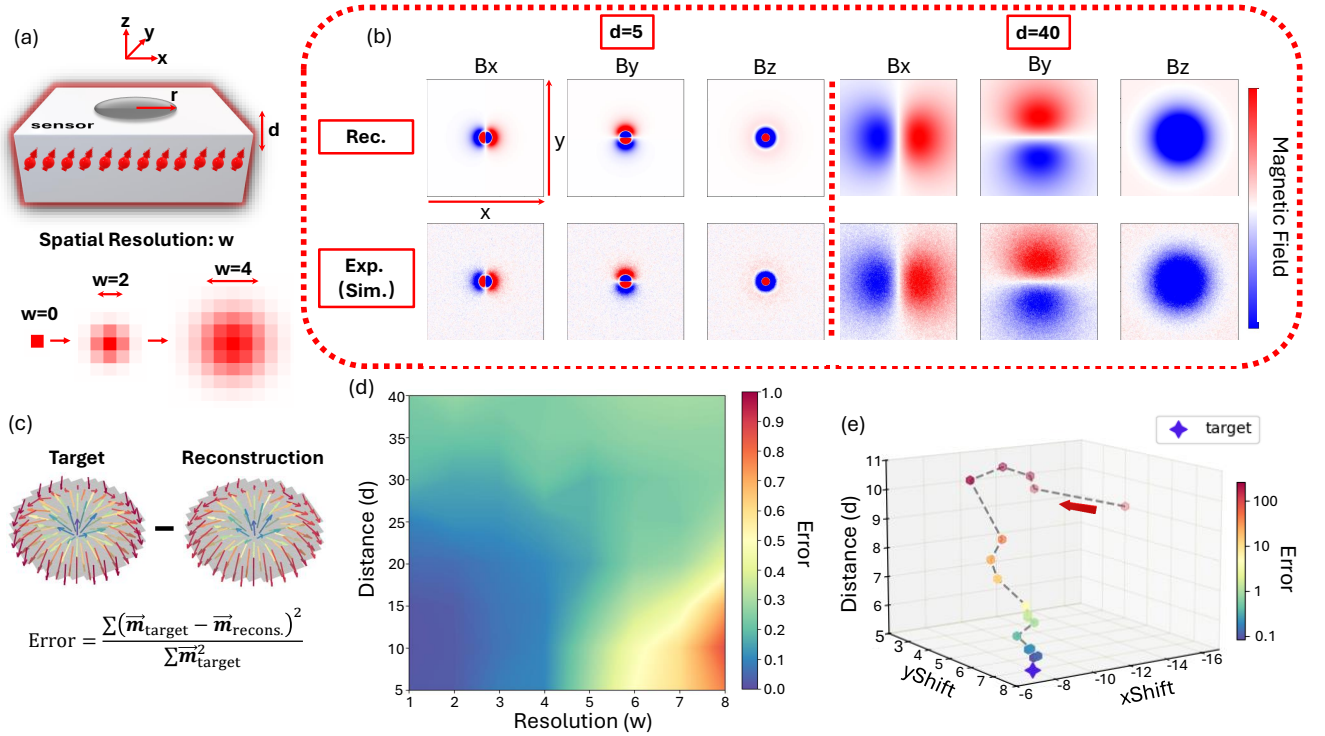


Figure 2. Case study of Néel-type skyrmion. (a) Schematic demonstration of the computational experiment setup, where  $d$  represents the sample-to-sensor distance,  $r$  is the skyrmion radius, and  $w$  is the full width at half maximum (FWHM) of a 2D Gaussian convolution, representing the experimental resolution. The skyrmion radius is fixed at  $r = 8$  throughout this study. (b) Comparison between the simulated experimental magnetic field and the reconstructed magnetic field at both large and small values of  $d$  (shown from left to right). All magnetic maps share the same scale, with dimensions of  $144 \times 144$ . (c) Demonstration of the error calculation. Here, the reconstructed magnetization is obtained with parameters  $d = 5$ ,  $w = 2$ , and SNR = 5. (d) Color map showing reconstruction error across different combinations of spatial resolution ( $w$ ) and sample-to-sensor distance ( $d$ ). (e) Visualization of the fitting process of experimental parameters with the 3D physical parameters, where each point represents a single optimization run, and the star denotes the target experimental parameters.

effective Hamiltonian tends to favor a continuous variation of spin directions [52, 53]. Even in the Heisenberg model with a negative exchange interaction  $J$  (representing anti-ferromagnetism systems), spin directions can change gradually when considering interactions beyond just nearest neighbors [54, 55], leading to smoother transitions across the lattice. The  $\beta$  term punishes large magnitudes of magnetization, resulting in a more average distribution, to avoid the physically unreasonable fluctuating distributions. Without  $\beta$  regularization, the optimization might assign an unphysically high value to a single pixel if this pixel can substantially reduce the error term, resulting in an incorrect representation. Typically, the  $\alpha$  and  $\beta$  terms act together, leading to faster convergence and smoother results.

Additionally, the tool allows for adding in prior assumptions of the real magnetization distributions in experiments. Here, we incorporate a topological  $\gamma$  term used when solving magnetic spin textures [56, 57]. A simple example is skyrmion, with topological charge  $Q = 1$ ,

which can be calculated in the continuous form:

$$Q = \frac{1}{4\pi} \int \mathbf{m} \cdot \left( \frac{\partial \mathbf{m}}{\partial x} \times \frac{\partial \mathbf{m}}{\partial y} \right) dx dy, \quad (5)$$

or in the discrete form:

$$Q = \frac{1}{4\pi} \sum_{x,y} \mathbf{m}_{\mathbf{r}} \cdot (\mathbf{m}_{\mathbf{r}+\hat{x}} \times \mathbf{m}_{\mathbf{r}+\hat{y}}). \quad (6)$$

In the reconstruction process, the error term in the loss function should dominate, and we need physical regularization parameters ( $\alpha$ ,  $\beta$ , and  $\gamma$ ) to guide the reconstruction without overshadowing the error term. In a reasonably noisy environment where the error term is typically around  $10^{-2}$ , the regularization parameters are empirically selected to be significantly smaller to ensure optimal reconstruction performance. For instance, in Figure 3(a),  $\alpha$  and  $\beta$  are set to  $2 \times 10^{-5}$  for the multi-domain ferromagnetism case. Similarly, in Figure 3(b),  $\alpha$  and  $\beta$  are set to  $2 \times 10^{-5}$ , while  $\gamma$  is  $8 \times 10^{-3}$  for the Néel-type skyrmion case with  $Q = 1$ . The reconstruction results remain robust against small variations in these empirical values.

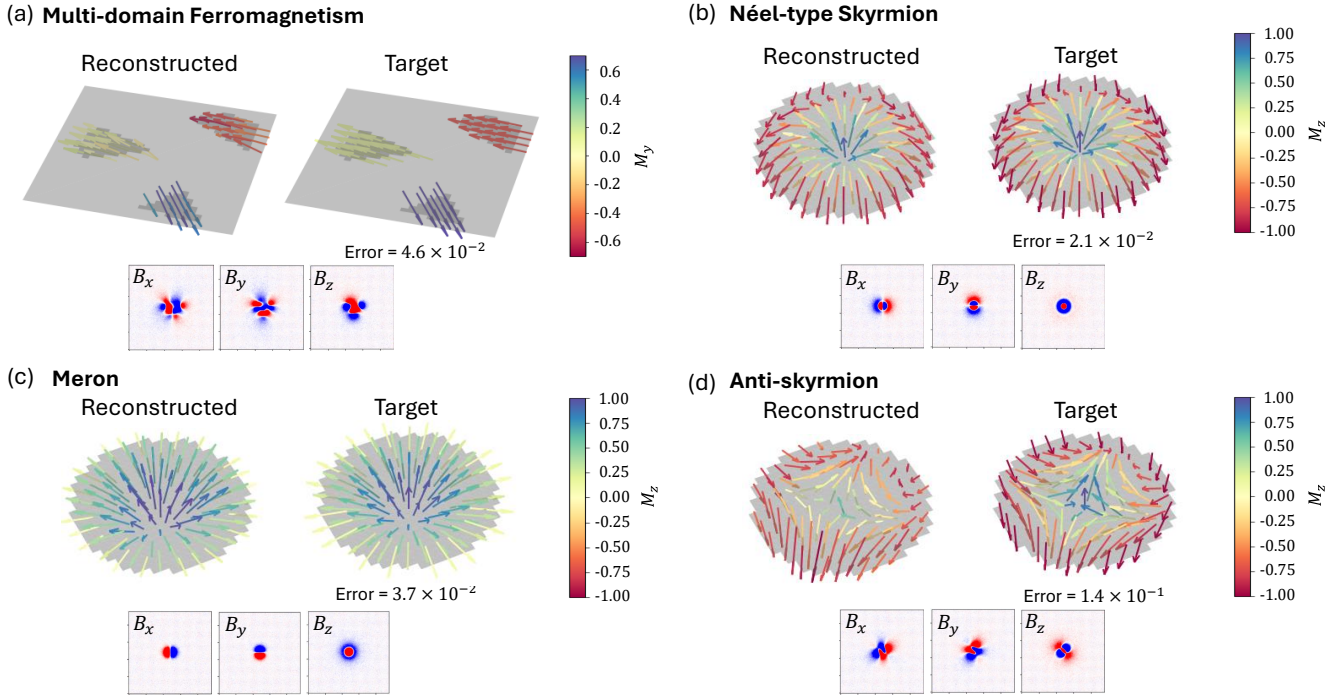


Figure 3. Comparison between target and reconstructed magnetization for various spin configurations. The magnetic field was measured at  $d = 5$  with an optical resolution  $w = 2$  and an SNR of 5 and shown below the magnetization. (a) Ferromagnetic regions, each with distinct randomly assigned uniform magnetization, separated by a distance of approximately 10. (b~d) Topological charge reconstruction for samples with a radius of 8. (b) Néel-type skyrmion with topological charge  $Q = 1$ . (c) Meron with  $Q = 1/2$ . (d) Anti-skyrmion with  $Q = -1$ .

Figure 1(b) shows the flow chart of our reconstruction model. It uses an experimentally measured vector magnetic field map, an assigned magnetization region, and defined spatial parameters as inputs and runs an optimization using the stochastic directional Newton's method. The process is then guided by the defined loss function, enabling the magnetization to rapidly converge to a physically meaningful result.

### CASE STUDY

In this section, we use a Néel-type skyrmion of radius  $r = 8$  as a demonstration. As shown in Figure 2(a), the sample of radius  $r$  is placed at a distance of  $d$  from the sensor plane. In experiments, measurement noise and finite spatial resolution are inherent in the sensed field maps. To mimic these experimental conditions, we apply Gaussian noise with a signal-to-noise ratio (SNR) of 5 to account for the measurement noise and incorporate finite spatial resolution using spatial Gaussian convolution with a full-width-half-maximum (FWHM) of  $w$ . The resulting field maps are then input into the model for reconstruction. As shown in Figure 2(c), we define a re-

construction error

$$\text{Error} = \frac{\sum (\vec{m}_{\text{target}} - \vec{m}_{\text{recons.}})^2}{\sum \vec{m}_{\text{target}}^2}$$

to quantify the fidelity of the reconstruction.

The success of magnetization reconstruction is closely linked to the amount of magnetic information present in the field maps. Experimentally, the quality of this information is mainly influenced by three factors: noise level, spatial resolution, and the distance from the source. While noise levels in sensing experiments can typically be reduced through extended averaging, tuning distance and spatial resolution in an in-situ setting is often challenging. As shown in Figure 2(d), we simulate the reconstruction process across various combinations of  $w$  and  $d$ , revealing that for a given spatial resolution constraint, there is an optimal distance at which spin configuration imaging yields the best results. With high spatial resolution ( $w \lesssim \frac{r}{2}$  in the case of an  $r = 8$  Néel-type skyrmion), comparable to the resolution of scanning NV microscopy ( $\sim 20\text{nm}$ ) [13, 58, 59], relative to the Néel-type skyrmion size ( $\sim 10^2\text{nm}$ ) [60–63], the reconstruction performs exceptionally well within  $d \lesssim 4r$ . In contrast, with low spatial resolution ( $w \gtrsim \frac{r}{2}$ ), as is typical for wide-field NV microscopy, the reconstruction can sometimes benefit from measurements taken at greater  $d$ . This phe-

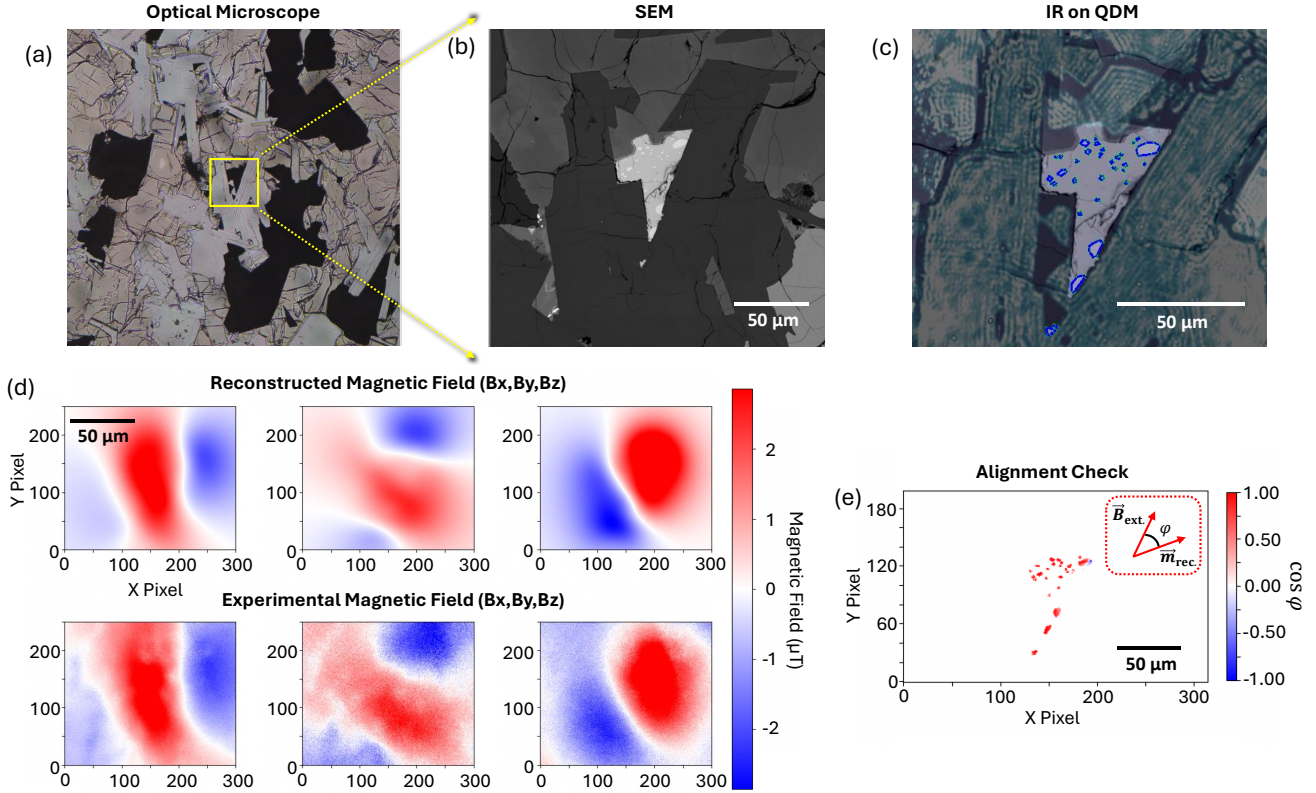


Figure 4. (a) Optical microscope image of the moon rock sample 10003,184, with the yellow frame highlighting the region selected for subsequent SEM imaging. (b) Backscattered SEM image showing the precise locations of potential magnetic rocks, visible as bright phases. (c) Infrared (IR) image acquired using the wide-field NV setup, covering the area where magnetic field measurements were performed. The IR image is overlaid on the SEM image, with the circled spots corresponding to the white spots in the SEM image, indicating the locations of magnetic sources (assigned magnetization region). (d) Comparison of experimental magnetic field data with reconstructed magnetic field components, displaying  $B_x$ ,  $B_y$ , and  $B_z$  from left to right. Measurements were conducted at room temperature with an external magnetic field applied in the direction of  $(-1.07, -0.74, 0.65)$  mT. (e)  $\cos \varphi$  map showing the alignment between the reconstructed magnetization vector and the expected direction (aligned with the applied field). As shown in the inset,  $\varphi$  is defined as the angle between reconstructed magnetization and the applied external magnetic field at each pixel.

nomenon is illustrated more clearly in Figure 2(b). In the left part of Figure 2(b), where measurements are taken very close to the sensor plane, fine magnetic features appear highly localized within a small region of the field maps. In this scenario, as the FWHM of the spatial Gaussian convolution increases, magnetic information rapidly deteriorates, leading to significant deviations in the reconstruction from the expected result. For magnetic imaging performed at greater sample-to-sensor distances, the magnetic information generally becomes more obscured as illustrated in the right part of Figure 2(b): most fine structures are lost, with only the lowest-order non-zero multipole term contributing. However, as the spatial scale of the magnetic field increases, the imaging becomes less vulnerable to resolution limits than in close measurements. This understanding suggests that recon-

struction may sometimes benefit from high-distance measurements, particularly when resolution limits are significant.

Our tool also supports physical parameter fitting for systems where distances and displacements are unknown or difficult to measure directly. To verify the accuracy of the fitting, we performed an additional simulation with the Néel-type case study. Figure 2(e) shows the results where all three parameters (distance,  $x_{\text{Shift}}$ , and  $y_{\text{Shift}}$ ) are fitted simultaneously. With each iteration, the parameters converge to the target value that we've assigned to represent unknown experimental parameters. Notably, the reconstruction error decreases with each iteration: reconstructed spin configuration becomes increasingly similar to the target configuration, demonstrating the successful information extraction from magnetic field mea-

surements.

## UNIVERSALITY DEMONSTRATION

In this section, we showcase the universal applicability of the developed model by applying it to diverse magnetization configurations, as shown in Figure 3. Additionally, we demonstrate that by adjusting the topological parameters ( $\gamma$ ), our model effectively captures a range of spin textures. From Figure 2(d), we gain a general understanding of the acceptable combinations of  $w$  and  $d$  needed for accurate magnetization reconstruction. Here, we set the experimental parameters to  $w = 2$ ,  $d = 5$ , and  $\text{SNR} = 5$  for all simulations.

Figure 3(a) shows the reconstruction of a three-domain ferromagnetic sample, where each domain is assigned a random magnetization. This configuration is common in ferromagnetic materials [64]. The average distance between the domains is approximately 10. Despite some degree of cancellation from oppositely oriented magnetization domains, our model accurately reconstructs the magnetization. Figures 3(b~d) depict the reconstruction of three distinct spin textures, each with a different topological charge. The spin texture region has a radius of 8. Figure 3(b) shows a Néel-type skyrmion with a topological charge  $Q = 1$ . Figure 3(c) is a Meron with  $Q = 1/2$ . Figure 3(d) is an anti-skyrmion with  $Q = -1$ . These results highlight the versatility of our computational model, as it is able to adjust to different topological instructions by modifying the  $Q$  values in the loss function. All reconstructions successfully capture the key features of the target spin configurations, demonstrating that our model is capable of reconstructing a wide range of source quantities.

Notice that the anti-skyrmion reconstruction exhibits a higher error compared to the other three cases, primarily due to the violation of the  $\beta$  condition in the anti-skyrmion configuration. While the anti-skyrmion maintains the same level of continuity as the skyrmion, its magnetic field contributions from different regions tend to cancel each other out to a larger extent. A magnetization distribution with smaller cancellations generates a magnetic field of relatively larger magnitude. To counteract this, the  $\beta$  regulation guides the optimization toward a magnetization distribution with a smaller overall magnitude. This trade-off between the positive and negative effects of  $\beta$  in this specific scenario ultimately results in an increase in the defined error.

## EXPERIMENTAL DEMONSTRATION

We showcase the complete reconstruction process by applying our model to the magnetization reconstruction of the Apollo lunar mare basalt sample 10003,184. Lu-

nar mineralogy and paleomagnetic research indicate that the predominant magnetic carriers in mare basalts are multi-domain metallic FeNi alloys, specifically kamacite (containing less than 5% Ni) and martensite (5-25% Ni) [65]. In this sample, we identify kamacite grains smaller than 50  $\mu\text{m}$ , which are associated with troilite (FeS) in a eutectic assemblage, using a Scanning Electron Microscope (SEM). Transmission electron microscopy (TEM) analysis of these kamacite grains contains nanoscale sub-grains or revealed defects or nanoscale sub-grains [66]. The sizes of these grains and sub-grains align with the single-domain (SD) to multi-domain (MD) spectrum [67]. Here, we identify these ferromagnetic species within the optical field of view, and we are able to generate magnetization results that align with the paleomagnetic understanding using vector magnetic field maps obtained through wide-field NV microscopy.

Figure 4 presents both the optical (a) and backscatter SEM image (b) of magnetic minerals observed in our lunar sample. The bright phases in the backscatter SEM image are identified as kamacite grains, potentially containing defects or nanoscale sub-grains. These grains are also visible in the infrared-light optical image captured by the camera in our wide-field NV microscopy setup (Figure 4(c)). By targeting the same field of view, we are able to accurately map and pinpoint the precise locations of the magnetic sources (the circled areas). Continuous optically detected magnetic resonance (ODMR) measurements are then performed to obtain the local magnetic fields generated by the lunar rock sample near the diamond surface under an applied field.

In our experiments, lunar rock samples are glued into a 3-*mm* thin section instead of being directly transferred to the diamond surface, making it difficult to measure the exact distance from the magnetic source to the NV plane. The focal planes for fluorescence and optical images often differ in NV sensing experiments, requiring z-axis adjustments to capture high-quality fluorescence images after locating the region of interest in the optical image, which will inevitably introduce some in-plane shifts. To address these challenges, we apply our parameter fitting and find x- and y-shifts of approximately (12, 2)  $\mu\text{m}$  and an optimized distance of around 27  $\mu\text{m}$ , which aligns with our rough optical measurements.

Starting from the optimized experimental parameters, we conduct the optimization procedures. Within 10 minutes of computation on an NVIDIA GeForce RTX 4070, our model produces a converged result for a total magnetization pixel number (number of  $p$ ) of 400. Figure 4(d) shows the near-perfect reconstruction of experimental magnetic field maps. Additionally, we demonstrate in Figure 4(e) that the reconstructed magnetization is well aligned with the applied field direction, consistent with our paleomagnetic expectation for these agnetic rocks.

## DISCUSSION

In this work, we develop a computational model designed for the universal reconstruction of magnetization configurations from magnetic field maps. Our approach is structured to leverage GPU acceleration, incorporating a physics-informed, customizable loss function to ensure physically meaningful outcomes. Compared to existing methods, our approach offers clear advantages: it requires little to no prior knowledge of the magnetic source, can be customized for different levels of prior information, and enables rapid computation of the full vector magnetization across a two-dimensional plane.

This tool enables the accurate determination of spatial measurement parameters that are otherwise challenging to obtain experimentally. After optimizing these parameters, one can first run the algorithm without prior assumptions to achieve a reasonable initial result. Then, based on insights gained from this initial optimization, the loss function can be adjusted to refine the solution toward a physically meaningful outcome. Additionally, the tool allows for simulating magnetization reconstruction across different noise levels, spatial resolution limits, and sample-to-sensor distances, helping to identify the optimal experimental conditions. With these capabilities, the computational model offers significant values for a broad spectrum of magnetic imaging experiments across different fields of study.

- 
- [1] Žutić, I., Fabian, J. & Sarma, S. D. Spintronics: Fundamentals and applications. *Reviews of modern physics* **76**, 323 (2004).
- [2] Barman, A., Mondal, S., Sahoo, S. & De, A. Magnetization dynamics of nanoscale magnetic materials: A perspective. *Journal of Applied Physics* **128** (2020).
- [3] Glenn, D. R. *et al.* Micrometer-scale magnetic imaging of geological samples using a quantum diamond microscope. *Geochemistry, Geophysics, Geosystems* **18**, 3254–3267 (2017).
- [4] Degen, C. L., Reinhard, F. & Cappellaro, P. Quantum sensing. *Reviews of modern physics* **89**, 035002 (2017).
- [5] Aslam, N. *et al.* Quantum sensors for biomedical applications. *Nature Reviews Physics* **5**, 157–169 (2023).
- [6] Li, J. *et al.* Serf atomic magnetometer—recent advances and applications: A review. *IEEE Sensors Journal* **18**, 8198–8207 (2018).
- [7] Patton, B., Zhivun, E., Hovde, D. & Budker, D. All-optical vector atomic magnetometer. *Physical review letters* **113**, 013001 (2014).
- [8] Romalis, M. V. & Dang, H. B. Atomic magnetometers for materials characterization. *Materials today* **14**, 258–262 (2011).
- [9] Fabricant, A., Novikova, I. & Bison, G. How to build a magnetometer with thermal atomic vapor: a tutorial. *New Journal of Physics* **25**, 025001 (2023).
- [10] Robbes, D. Highly sensitive magnetometers—a review. *Sensors and Actuators A: Physical* **129**, 86–93 (2006).
- [11] Cai, B. *et al.* Herriott-cavity-assisted all-optical atomic vector magnetometer. *Physical Review A* **101**, 053436 (2020).
- [12] Huang, H., Dong, H., Chen, L. & Gao, Y. Single-beam three-axis atomic magnetometer. *Applied Physics Letters* **109** (2016).
- [13] Maletinsky, P. *et al.* A robust scanning diamond sensor for nanoscale imaging with single nitrogen-vacancy centres. *Nature nanotechnology* **7**, 320–324 (2012).
- [14] Casola, F., Van Der Sar, T. & Yacoby, A. Probing condensed matter physics with magnetometry based on nitrogen-vacancy centres in diamond. *Nature Reviews Materials* **3**, 1–13 (2018).
- [15] Hsieh, S. *et al.* Imaging stress and magnetism at high pressures using a nanoscale quantum sensor. *Science* **366**, 1349–1354 (2019).
- [16] Glenn, D. R. *et al.* Single-cell magnetic imaging using a quantum diamond microscope. *Nature methods* **12**, 736–738 (2015).
- [17] Barry, J. F. *et al.* Sensitivity optimization for nv-diamond magnetometry. *Reviews of Modern Physics* **92**, 015004 (2020).
- [18] Gross, I. *et al.* Direct measurement of interfacial dzyaloshinskii-moriya interaction in x—cofeb—mgo heterostructures with a scanning nv magnetometer (x= ta, tan, and w). *Physical Review B* **94**, 064413 (2016).
- [19] Levine, E. V. *et al.* Principles and techniques of the quantum diamond microscope. *Nanophotonics* **8**, 1945–1973 (2019).
- [20] Bhattacharyya, P. *et al.* Imaging the meissner effect in hydride superconductors using quantum sensors. *Nature* **627**, 73–79 (2024).
- [21] Davis, E. J. *et al.* Probing many-body dynamics in a two-dimensional dipolar spin ensemble. *Nature physics* **19**, 836–844 (2023).
- [22] Gottscholl, A. *et al.* Initialization and read-out of intrinsic spin defects in a van der waals crystal at room temperature. *Nature materials* **19**, 540–545 (2020).
- [23] Gottscholl, A. *et al.* Room temperature coherent control of spin defects in hexagonal boron nitride. *Science Advances* **7**, eabf3630 (2021).
- [24] Healey, A. *et al.* Quantum microscopy with van der waals heterostructures. *Nature Physics* **19**, 87–91 (2023).
- [25] Gong, R. *et al.* Coherent dynamics of strongly interacting electronic spin defects in hexagonal boron nitride. *Nature Communications* **14**, 3299 (2023).
- [26] Vaidya, S., Gao, X., Dikshit, S., Aharonovich, I. & Li, T. Quantum sensing and imaging with spin defects in hexagonal boron nitride. *Advances in Physics: X* **8**, 2206049 (2023).
- [27] Gong, R. *et al.* Isotope engineering for spin defects in van der waals materials. *Nature Communications* **15**, 104 (2024).
- [28] Kleiner, R., Koelle, D., Ludwig, F. & Clarke, J. Superconducting quantum interference devices: State of the art and applications. *Proceedings of the IEEE* **92**, 1534–1548 (2004).
- [29] Cohen, D. Magnetoencephalography: detection of the brain’s electrical activity with a superconducting magnetometer. *Science* **175**, 664–666 (1972).
- [30] Enpuku, K. *et al.* Detection of magnetic nanoparticles with superconducting quantum interference device (squid) magnetometer and application to immunoassays.

- Japanese journal of applied physics* **38**, L1102 (1999).
- [31] Cohen, D., Edelsack, E. A. & Zimmerman, J. E. Magnetocardiograms taken inside a shielded room with a superconducting point-contact magnetometer. *Applied Physics Letters* **16**, 278–280 (1970).
- [32] Drung, D., Cantor, R., Peters, M., Scheer, H. & Koch, H. Low-noise high-speed dc superconducting quantum interference device magnetometer with simplified feedback electronics. *Applied physics letters* **57**, 406–408 (1990).
- [33] Xu, Y., Zhang, W. & Tian, C. Recent advances on applications of nv- magnetometry in condensed matter physics. *Photonics Research* **11**, 393–412 (2023).
- [34] Liu, J. *et al.* Magnetic skyrmionic bubbles at room temperature and sign reversal of the topological hall effect in a layered ferromagnet cr0. 87te. *ACS nano* **16**, 13911–13918 (2022).
- [35] Fragkos, S., Pappas, P., Symeonidou, E., Panayiotatos, Y. & Dimoulas, A. Magnetic skyrmion manipulation in crte2/wte2 2d van der waals heterostructure. *Applied Physics Letters* **120** (2022).
- [36] Dovzhenko, Y. *et al.* Magnetostatic twists in room-temperature skyrmions explored by nitrogen-vacancy center spin texture reconstruction. *Nature communications* **9**, 2712 (2018).
- [37] Ichkitidze, L., Bazaev, N., Telyshev, D., Preobrazhensky, R. & Gavrushina, M. Magnetic field sensors in medical diagnostics. *Biomedical Engineering* **48**, 305–309 (2015).
- [38] Zhang, T. *et al.* Toward quantitative bio-sensing with nitrogen–vacancy center in diamond. *ACS sensors* **6**, 2077–2107 (2021).
- [39] Le Sage, D. *et al.* Optical magnetic imaging of living cells. *Nature* **496**, 486–489 (2013).
- [40] Fu, R. R., Lima, E. A., Volk, M. W. & Trubko, R. High-sensitivity moment magnetometry with the quantum diamond microscope. *Geochemistry, Geophysics, Geosystems* **21**, e2020GC009147 (2020).
- [41] Lima, E. A. & Weiss, B. P. Ultra-high sensitivity moment magnetometry of geological samples using magnetic microscopy. *Geochemistry, Geophysics, Geosystems* **17**, 3754–3774 (2016).
- [42] Lima, E. A. & Weiss, B. P. Obtaining vector magnetic field maps from single-component measurements of geological samples. *Journal of Geophysical Research: Solid Earth* **114** (2009).
- [43] Steele, S. C. *et al.* Paleomagnetic evidence for a long-lived, potentially reversing martian dynamo at  $\sim 3.9$  ga. *Science Advances* **9**, eade9071 (2023).
- [44] Roth, B. J., Sepulveda, N. G. & Wikswo Jr, J. P. Using a magnetometer to image a two-dimensional current distribution. *Journal of applied physics* **65**, 361–372 (1989).
- [45] Broadway, D. *et al.* Improved current density and magnetization reconstruction through vector magnetic field measurements. *Physical Review Applied* **14**, 024076 (2020).
- [46] Dubois, A. E. *et al.* Untrained physically informed neural network for image reconstruction of magnetic field sources. *Physical Review Applied* **18**, 064076 (2022).
- [47] Ghasemifard, F., Johansson, M. & Norgren, M. Current reconstruction from magnetic field using spherical harmonic expansion to reduce impact of disturbance fields. *Inverse Problems in Science and Engineering* **25**, 795–809 (2017).
- [48] Reed, N. R. *et al.* Machine learning for improved current density reconstruction from 2d vector magnetic images. *arXiv preprint arXiv:2407.14553* (2024).
- [49] Saha, R. *et al.* Observation of néel-type skyrmions in acentric self-intercalated cr1+  $\delta$ te2. *Nature Communications* **13**, 3965 (2022).
- [50] Yao, C. & Shi, Y. Magrec. <https://github.com/ycy-ycy/MagRec> (2024). Accessed: 2024-11-13.
- [51] Lima, E. A., Irimia, A. & Wikswo, J. P. The magnetic inverse problem. *The SQUID handbook: applications of SQUIDs and SQUID systems* 139–267 (2006).
- [52] Newell, G. F. & Montroll, E. W. On the theory of the ising model of ferromagnetism. *Reviews of Modern Physics* **25**, 353 (1953).
- [53] Katsura, S. Statistical mechanics of the anisotropic linear heisenberg model. *Physical Review* **127**, 1508 (1962).
- [54] Scholl, A. *et al.* Observation of antiferromagnetic domains in epitaxial thin films. *Science* **287**, 1014–1016 (2000).
- [55] Shpyrko, O. *et al.* Direct measurement of antiferromagnetic domain fluctuations. *Nature* **447**, 68–71 (2007).
- [56] Yin, G. *et al.* Topological charge analysis of ultrafast single skyrmion creation. *Physical Review B* **93**, 174403 (2016).
- [57] Rybakov, F. N. & Kiselev, N. S. Chiral magnetic skyrmions with arbitrary topological charge. *Physical review B* **99**, 064437 (2019).
- [58] Zhou, T. X., Stöhr, R. J. & Yacoby, A. Scanning diamond nv center probes compatible with conventional afm technology. *Applied Physics Letters* **111** (2017).
- [59] Arai, K. *et al.* Fourier magnetic imaging with nanoscale resolution and compressed sensing speed-up using electronic spins in diamond. *Nature nanotechnology* **10**, 859–864 (2015).
- [60] Wu, Y. *et al.* Néel-type skyrmion in wte2/fe3gete2 van der waals heterostructure. *Nature communications* **11**, 3860 (2020).
- [61] Park, T.-E. *et al.* Néel-type skyrmions and their current-induced motion in van der waals ferromagnet-based heterostructures. *Physical Review B* **103**, 104410 (2021).
- [62] Wang, X., Yuan, H. & Wang, X. A theory on skyrmion size. *Communications Physics* **1**, 31 (2018).
- [63] Romming, N., Kubetzka, A., Hanneken, C., von Bergmann, K. & Wiesendanger, R. Field-dependent size and shape of single magnetic skyrmions. *Physical review letters* **114**, 177203 (2015).
- [64] Taniuchi, T. *et al.* Imaging of room-temperature ferromagnetic nano-domains at the surface of a non-magnetic oxide. *Nature Communications* **7**, 11781 (2016).
- [65] Weiss, B. P. & Tikoo, S. M. The lunar dynamo. *Science* **346**, 1246753 (2014).
- [66] Jung, J., Tikoo, S. M., Burns, D., Váci, Z. & Krawczynski, M. J. Assessing lunar paleointensity variability during the 3.9 - 3.5 ga high field epoch. *Earth and Planetary Science Letters* **638**, 118757 (2024).
- [67] Muxworthy, A. R. & Williams, W. Critical single-domain grain sizes in elongated iron particles: implications for meteoritic and lunar magnetism. *Geophysical Journal International* **202**, 578–583 (2015).